PIEZOELECTRICS

Giant piezoelectricity in oxide thin films with nanopillar structure

Huajun Liu[1]*†, Haijun Wu[2]†, Khuong Phuong Ong[3], Tiannan Yang[4], Ping Yang[2,5], Pranab Kumar Das[5], Xiao Chi[6], Yang Zhang[2], Caozheng Diao[5], Wai Kong Alaric Wong[5], Eh Piew Chew[5], Yi Fan Chen[1], Chee Kiang Ivan Tan[1], Andrivo Rusydi[6], Mark B. H. Breese[5,6], David J. Singh[7], Long-Qing Chen[4], Stephen J. Pennycook[2], Kui Yao[1]*

High-performance piezoelectric materials are critical components for electromechanical sensors and actuators. For more than 60 years, the main strategy for obtaining large piezoelectric response has been to construct multiphase boundaries, where nanoscale domains with local structural and polar heterogeneity are formed, by tuning complex chemical compositions. We used a different strategy to emulate such local heterogeneity by forming nanopillar regions in perovskite oxide thin films. We obtained a giant effective piezoelectric coefficient $d^*_{33,f}$ of ~1098 picometers per volt with a high Curie temperature of ~450°C. Our lead-free composition of sodium-deficient sodium niobate contains only three elements (Na, Nb, and O). The formation of local heterogeneity with nanopillars in the perovskite structure could be the basis for a general approach to designing and optimizing various functional materials.

The well-established strategy for achieving high piezoelectric performance is to construct multiphase boundaries by tuning complex chemical compositions, such as the morphotropic phase boundary in lead zirconate titanate (PZT) (*1*) or the polymorphic phase boundary in potassium sodium niobate (KNN) (*2*). At these phase boundaries, energy differences among the distinct crystalline phases are adequately small with flattened thermodynamic energy profiles, giving rise to low domain wall energy and miniaturization of ferroelectric domains (*3*, *4*). The local structural and chemical heterogeneity at the nanoscale is recognized to play a key role in achieving ultrahigh piezoelectric coefficients (*5*–*7*). However, the strategy of constructing composition-controlled phase boundaries usually involves complex chemical compositions, and these often have poor temperature stability due to a substantially reduced Curie temperature (T_C) from extensive doping.

Defects, such as dislocations and dopants, are important for developing materials with certain properties, such as the mechanical properties of metals or the electronic properties of semiconductors. An out-of-phase boundary is a type of extended crystallographic defect characterized by a misregistry of a fraction of a unit cell dimension in neighboring regions of a crystal (*8*). When the offset of the misregistry is a half of a unit cell dimension, it is the special case known as the antiphase boundary (*8*, *9*). Although the origins of out-of-phase boundaries and their influences on properties have been well studied in metal alloys (*10*) and semiconductor thin films (*11*), their investigation in complex oxides is rare (*9*) and their link to functional properties remains elusive (*8*). We show that the out-of-phase boundaries between the nanopillar regions and regular perovskite matrix induce local structural and polar heterogeneity and emergent giant piezoelectric response in lead-free, Na-deficient $NaNbO_3$ thin films. We used atomic-scale images to reveal the formation of vertical nanopillars with size of a few to tens of nanometers. The structural distortions around nanopillar regions lower the crystal symmetry from tetragonal to monoclinic structure, facilitating polarization rotation and domain wall motion under electric fields to substantially enhance piezoelectric performance as supported by theoretical calculations. We discovered a giant effective piezoelectric coefficient $d^*_{33,f}$ of ~1098 pm/V at 1 kHz with an applied electric field of 125 kV/cm, which is more than twice that of the best PZT films (*12*) and four times that of the best KNN-based films with extensive doping (*13*). We maintained a simple composition of three elements (Na, Nb, and O) and a high T_C of ~450°C.

We grew epitaxial thin films of stoichiometric $NaNbO_3$ (NNO) with regular perovskite structure and Na-deficient NNO with nanopillar regions (NPR-NNO) on Nb-doped $SrTiO_3$ (001) substrates by sputter deposition (*14*). Our stoichiometric NNO film was homogeneous with a thickness of ~200 nm, which we determined using a low-magnification annular bright field (ABF) image taken by scanning transmission electron microscopy (STEM) (Fig. 1A). The Nb atoms are arranged in a typical perovskite lattice (Fig. 1, B and C). In contrast, we found vertically aligned nanopillars with a smooth surface in the cross-sectional view of NPR-NNO film (Fig. 1D). Those nanopillars are embedded in the matrix of regular perovskite structure. Inside the nanopillar regions, the Nb atoms occupy the original Na positions along both in-plane directions (Fig. 1H), and the Na atoms also occupy the original Nb positions along both in-plane directions (fig. S2B). In the cross-sectional view (Fig. 1E), we observed many extended columnar structures. By changing the microscope focus, we confirm that these columnar structures are nanoscale in in-plane dimensions (fig. S1), fully consistent with the nanoscale size of nanopillar regions ranging from a few to tens of nanometers in the plan-view image (Fig. 1G). Because the thickness of the sample greatly exceeds the thickness of the nanopillars, we actually see overlapping of the nanopillar regions (marked by arrows in Fig. 1E) and the matrix. The lattice in the nanopillar regions (yellow box in Fig. 1, E and H) is shifted slightly by δ_C along the out-of-plane direction and by approximately half of a unit cell along both in-plane directions from the lattice of the matrix (red box in Fig. 1, E and H). Hence, the misregistry between the nanopillar regions and matrix can be seen as normal perovskite phase shifted by $\langle \mathbf{a}/2, \mathbf{b}/2, \boldsymbol{\delta}_C \rangle$, where $\mathbf{a}$ and $\mathbf{b}$ are unit vectors along in-plane directions and $\boldsymbol{\delta}_C$ is along the out-of-plane direction with magnitude of a small fraction of the unit cell length. This boundary is an out-of-phase boundary, which is different from an antiphase boundary where the displacement vector would be $\langle \mathbf{a}/2, \mathbf{b}/2, \mathbf{c}/2 \rangle$.

On the basis of the above structure details, we constructed a schematic structural model (Fig. 1, F and I). At the out-of-phase boundary between the nanopillar regions and the matrix, the oxygen octahedra are edge-sharing instead of the corner-sharing octahedra normally found in perovskites. Analogous to the Ruddlesden-Popper stacking faults in perovskite structures of ABO_3 with A-site excess (*15*), these out-of-phase boundaries can accommodate more Nb atoms than the stoichiometric perovskite (fig. S2). The Na deficiency (fig. S3) in the NPR-NNO film drives the formation of out-of-phase boundaries with atoms sitting at in-plane antisite positions (Fig. 1, H and I). The interface atomic structure between the NPR-NNO film and the substrate (fig. S2G) shows that the first layer of film appears to be a Nb-occupied NaO layer, which largely determines the growth pattern of the nanopillar structures in the following layers. According to first-principles calculations (*14*), when Na is deficient and Nb is rich, the negative formation energy of antisite Nb_{Na} shows that it is energetically favorable for excess Nb atoms to occupy Na vacancies.

[1]Institute of Materials Research and Engineering, A*STAR (Agency for Science, Technology and Research), 138634 Singapore. [2]Department of Materials Science and Engineering, National University of Singapore, 117575 Singapore. [3]Institute of High Performance Computing, A*STAR (Agency for Science, Technology and Research), 138632 Singapore. [4]Department of Materials Science and Engineering, Pennsylvania State University, University Park, PA 16802, USA. [5]Singapore Synchrotron Light Source (SSLS), National University of Singapore, 117603 Singapore. [6]Department of Physics, National University of Singapore, 117551 Singapore. [7]Department of Physics and Astronomy, University of Missouri, Columbia, MO 65211, USA.
*Corresponding author. Email: huajunliu87@gmail.com (H.L.); k-yao@imre.a-star.edu.sg (K.Y.)
†These authors contributed equally to this work.

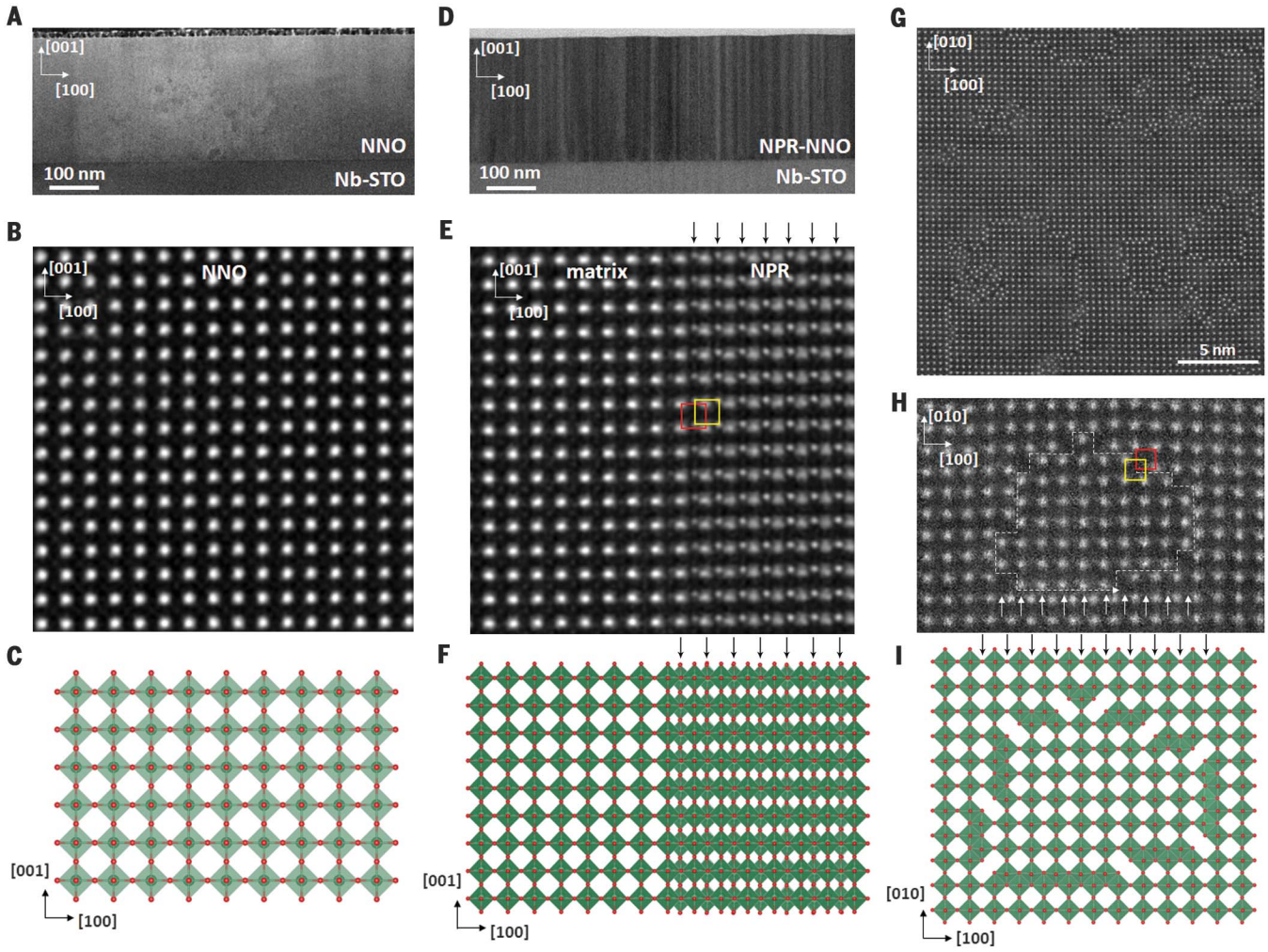

Fig. 1. Atomic structures of NNO and NPR-NNO thin films. (**A** to **C**) Cross-sectional low-magnification STEM ABF image (A), atomically resolved HAADF image (B), and schematic structural model (C) of NNO films on Nb-STO (001) substrates. (**D**, **E**, **G**, and **H**) Cross-sectional low-magnification ABF image (D), cross-sectional atomically resolved HAADF image (E), plan-view high-magnification image (G), and plan-view atomically resolved HAADF image (H) of NPR-NNO films on Nb-STO (001) substrates. (**F** and **I**) Schematic structural models of NPR-NNO films in cross-sectional view (F) and plan view (I). The arrows in (E), (F), (H), and (I) indicate the rows of Nb atoms in the nanopillar regions. They are much weaker than the Nb atom columns in the normal crystal from cross-sectional view [left side of (E)] because they are much shorter along the beam direction. The yellow and red boxes in (E) and (H) represent the lattice of the nanopillar region and the regular perovskite structure of the matrix, respectively. The dashed lines in (H) show the nanopillar region.

We used synchrotron x-ray diffraction to investigate the crystal structures and temperature-dependent phase transitions of the NNO and NPR-NNO films. The thickness fringes around the main diffraction (001) peak of the NPR-NNO film (Fig. 2A) reflect the high quality and smooth surface, whereas we observed no thickness fringes for NNO films. We found a single diffraction peak with the same in-plane lattice parameter as the Nb-STO substrate in the (103) reciprocal space mapping (RSM) for the NNO film (Fig. 2B). This indicates that the NNO film is coherently strained even at a thickness of 200 nm, and the observation is consistent with a previous report (*16*). This is probably due to the small lattice mismatch of ~0.47% between the NNO bulk structure and the Nb-STO substrate (fig. S4). Combined with other RSMs, we found that the NNO film has a tetragonal symmetry. However, the (103) RSM for the NPR-NNO film (Fig. 2C) shows peak splitting due to monoclinic symmetry (see fig. S4 for more RSMs and lattice parameters). Oxygen octahedral rotations in the perovskite structure give rise to doubling of the unit cell along certain directions, which can be probed by the half-order diffraction peaks (*17*) (Fig. 2D). The half-order (0 0.5 1.5) diffraction peak is equivalent to the (0.5 0 1.5) peak (fig. S4B) because of the isotropic nature of the in-plane directions of the Nb-STO substrate, thus suggesting that the in-phase rotation exists along both in-plane directions. According to Glazer's notation (*18*), the rotation patterns for both films are a mixture of $a^-b^+c^-$ and $a^+b^-c^-$. However, the NPR-NNO film shows substantially lower peak intensity, especially the (1.5 0.5 1.5) and (0.5 0.5 1.5) peaks corresponding to out-of-phase rotations. This is probably due to the distortion induced by the nanopillar regions and the edge-sharing octahedra at the out-of-phase boundary (Fig. 1, G to I) that breaks the long-range order of rotation.

We conducted temperature-dependent x-ray diffraction to study the phase transition (Fig. 2E). The out-of-plane lattice parameter c shows a change in slope at ~457°C for the NNO and NPR-NNO films. The changes in the in-plane lattice parameters a of both films are less obvious as a result of the constraint by the substrates. We also monitored the intensity of the half-order (0 0.5 1.5) diffraction peak (Fig. 2F). For both NNO and NPR-NNO films,

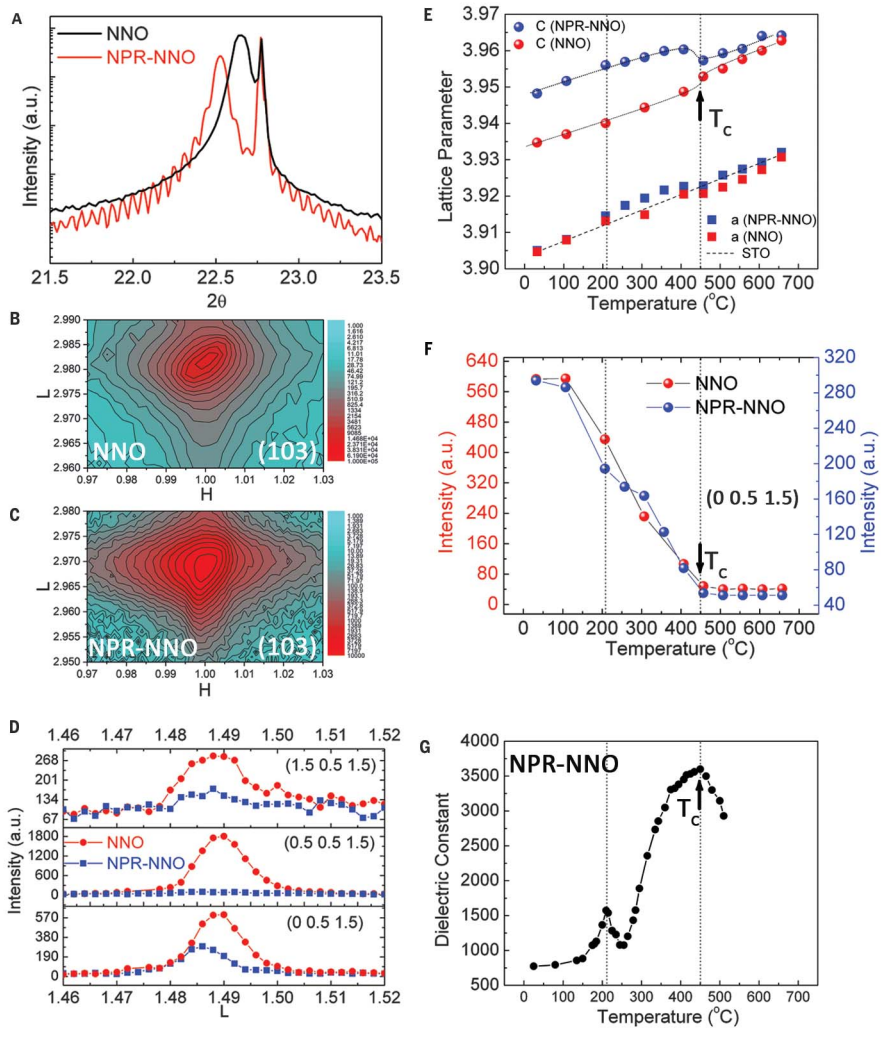

Fig. 2. Crystal structure and phase transition of NNO and NPR-NNO thin films. (**A**) X-ray diffraction patterns around the (001) peak for NNO and NPR-NNO films. (**B** and **C**) Reciprocal space mapping around the (103) peak for the NNO film (B) and the NPR-NNO film (C), plotted in reciprocal lattice units of the Nb-STO substrate. (**D**) Half-order diffraction peaks for the NNO and NPR-NNO films. (**E**) Lattice parameters of the NNO and NPR-NNO films as a function of temperature. (**F**) Intensity of the half-order (0 0.5 1.5) diffraction peaks as a function of temperature for the NNO and NPR-NNO films. (**G**) Dielectric constant measured at 1 kHz as a function of temperature for the NPR-NNO film.

the diffraction peaks disappear and the intensities decrease to the background level at ~457°C. This observation suggests a phase transition from the a^+ and b^+ tilt pattern to nontilted a^0 and b^0 of a higher symmetry phase, with the likely space group being *P4/mbm* above 457°C (*19*). Measuring the temperature dependence of the dielectric constant for the NPR-NNO film (Fig. 2G) shows a peak at ~450°C, confirming the high T_C. The smaller peak at ~210°C could be related to a ferroelectric-to-ferroelectric phase transition, as we observed no obvious structural change (Fig. 2, E and F). The hysteresis loops we measured demonstrate the ferroelectric nature of both films (fig. S5, A to C).

To investigate the macroscopic piezoelectric properties of the films, we used a laser scanning vibrometer (*20*–*22*) with an ac unipolar voltage of 2 V in magnitude at 1 kHz for the NNO film (Fig. 3A). We determined the effective piezoelectric coefficient $d^*_{33,f}$ to be ~22 pm/V based on the magnitude of the surface displacement. The electric field dependence of the piezoelectric coefficient and strain for the NNO film exhibits the linear dependence of strain on the electric field, as found in typical piezoelectric materials (Fig. 3B). We found no dependence of the piezoelectric coefficient on the driving frequency of the electric field for the NNO film (Fig. 3C), which agrees with the impedance spectroscopy results (fig. S5D). We measured the film displacement of the NPR-NNO film under the same conditions as the NNO film (Fig. 3D). We determined the effective piezoelectric coefficient $d^*_{33,f}$ to be ~1098 pm/V at 1 kHz with an applied electric field of 125 kV/cm (Fig. 4, E and F). The NPR-NNO film has nonlinear behavior and much-enhanced strain at a higher electric field (Fig. 3E). Decreasing the electric field leads to a very small strain hysteresis (Fig. 3E). This behavior departs from the strong hysteretic behavior of the point defect–induced large strain in aged $BaTiO_3$ single crystal (*23*). The effective piezoelectric strain of the NPR-NNO film increases nonlinearly with the electric field, saturating at ~1.4% above 125 kV/cm. We observed a strong dependence of the effective piezoelectric coefficient on the driving frequency of the electric field for the NPR-NNO film (Fig. 3F). At a low frequency of 100 Hz, the effective piezoelectric coefficient reaches a giant value of ~8114 pm/V, whereas it drops to ~112 pm/V at a high frequency of 10 kHz. The strain shows a similar strong dependence on frequency (see fig. S6). We believe that the strong amplitude and electric field frequency dependence of the piezoelectric strain of the NPR-NNO film indicates a substantial contribution from the motion of out-of-phase boundaries between nanopillar regions and the matrix perovskite (*24*). We observed a strong frequency dependence of dielectric constant and loss in NPR-NNO films in the impedance spectroscopy (fig. S5). X-ray absorption spectra (fig. S7) suggest a slightly occupied Nb 4d level in the NPR-NNO film as compared to the empty Nb 4d level in the NNO film, consistent with higher leakage in the NPR-NNO film (fig. S5F), which could come from the vertical boundaries of the nanopillar regions.

We performed first-principles calculations and phase-field simulations to better understand the mechanism of the giant piezoelectric response (*14*). We calculated the formation energy of the antisite Nb_{Na} defect as a function of chemical potential of Na under both Nb-deficient and Nb-rich conditions (Fig. 4A). The negative formation energy under Nb-rich and Na-deficient conditions shows that excess Nb atoms would occupy Na vacant positions to form antisite Nb_{Na} defects when NNO is Na-deficient. However, as a result of large differences between the ionic radii and valences of Na and Nb ions, antisite Nb atoms are not stable at the original antisite position but show substantial off-centering along the out-of-plane *c* direction. This behavior is similar to Sr-deficient $SrTiO_3$ thin films (*25*). First-principles calculations predict the energies of antisite Nb atoms at different positions (Fig. 4B), showing that large off-centering displacement is energetically favorable. The off-centering displacement induces a large ferroelectric polarization of ~16.2 μC/cm^2 along the out-of-plane *c* direction in the structure with antisite defects. This polarization is greatly enhanced from the polarization of ~1.2 μC/cm^2 in the regular

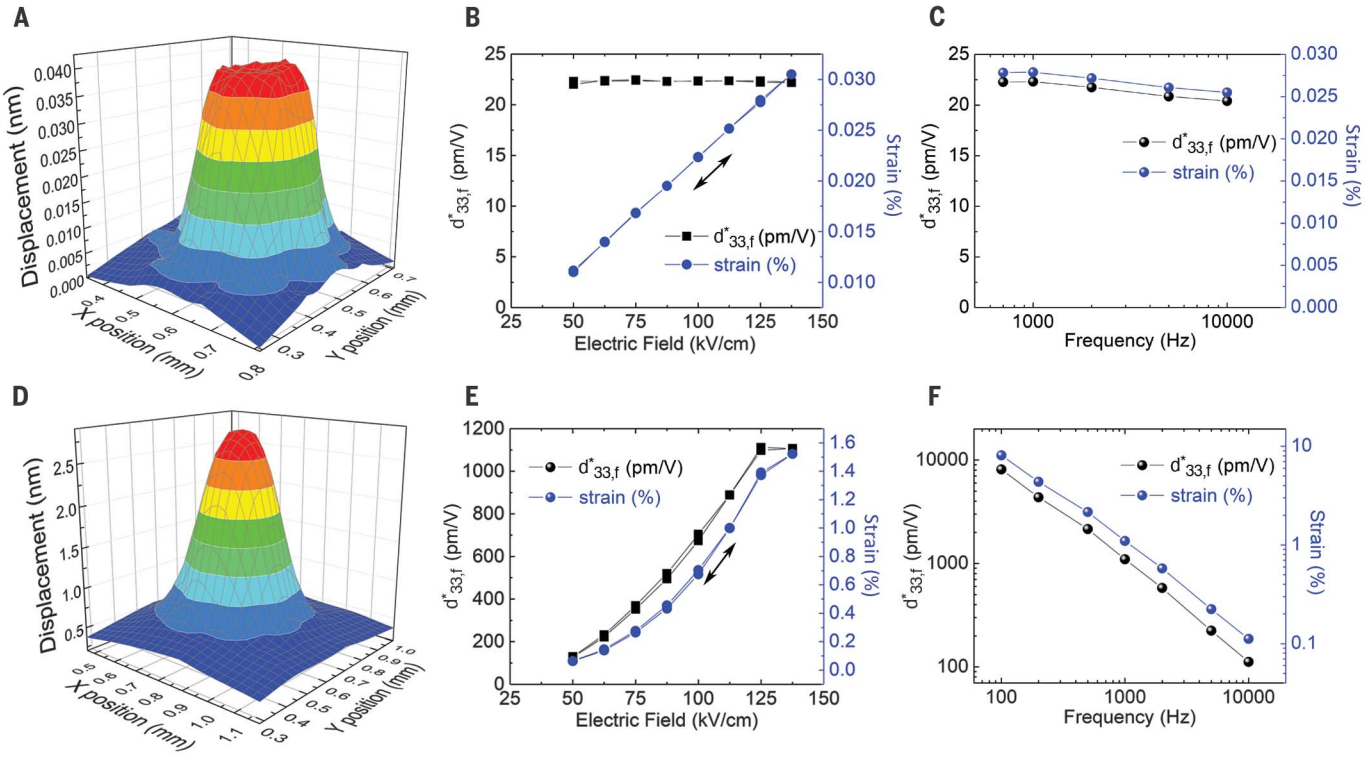

Fig. 3. Piezoelectric properties of NNO and NPR-NNO thin films. (**A** and **D**) 3D drawing of surface displacement of the NNO film (A) under ac unipolar voltage of 2 V in magnitude at 1 kHz and the NPR-NNO film (D) under ac unipolar voltage of 2.5 V in magnitude at 1 kHz. (**B** and **E**) Electric field dependence of effective piezoelectric coefficient and strain of the NNO film (B) and the NPR-NNO film (E) at frequency of 1 kHz. (**C** and **F**) Frequency dependence of effective piezoelectric coefficient and strain of the NNO film (C) and the NPR-NNO film (F).

perovskite structure of NNO, according to first-principles calculations. This large local polarization distorts the surrounding lattice to lower symmetry and gives rise to local polar heterogeneity at the nanoscale. However, the d_{33} we calculated by first principles from the piezoelectric stress tensor and elastic stiffness (*14*) is ~17 pm/V for the structural model with antisite defects and ~14 pm/V for the structural model of normal perovskite. The similar values indicate that the giant strain we observed in the experiments likely originates at a scale beyond the unit cells of the lattice.

We used phase-field simulations to study the contributions by nanopillar regions and their boundaries to the piezoelectric properties (*14*). We simulated the ferroelectric domain structure of the NPR-NNO film (fig. S9, C and D). The local stress developed around the boundaries of nanopillar regions (fig. S9E) causes the polarization directions to be rotated away from the out-of-plane direction, thus forming a multidomain structure with coexisting tetragonal *c* domains and nanoscale monoclinic domains with rich and mixed orientations of polarizations. We simulated the piezoelectric strain response to a static electric field applied along the out-of-plane direction (Fig. 4C). The tetragonal domains (e.g., region III in Fig. 4C) show a weak piezoelectric strain response, whereas the monoclinic domains (e.g., region I) show a much stronger response. The strongest piezoelectric strain response appears around the domain walls between tetragonal and monoclinic domains (e.g., region II). The motions of these domain walls under the electric field serve as substantial contributions to the piezoelectric response, giving rise to a factor of ~15 enhancement of the piezoelectric coefficient d_{33} ~ 290 pm/V for NPR-NNO film as compared with ~20 pm/V for pure NNO film from phase-field simulations. We simulated the frequency dependence of piezoelectric strain by applying an ac electric field at different frequencies (Fig. 4D). The domain wall motion is weakened upon increasing the frequency for the NPR-NNO film (fig. S9, F to H). The piezoelectric response of both the domain wall regions and the monoclinic domains decreases, while the piezoelectric response of the tetragonal domains is almost unchanged. For the NNO film with a single tetragonal domain, the piezoelectric strain is almost independent of frequency. Our simulation results suggest that the giant piezoelectric response is likely to originate from domain wall motion under electric fields. The substantially reduced domain wall response at high frequencies results in the strong frequency dependence of the piezoelectric property we observed.

Because the piezoelectric properties of ferroelectric materials are lost when the temperature exceeds T_C, a high T_C is preferred for applications. We compared the piezoelectric coefficient d_{33} of several major lead-free piezoelectric materials systems together with PZT ceramics as a function of T_C (Fig. 4E and fig. S10A). A common strategy to enhance the piezoelectric coefficient in bulk ceramics is to construct phase boundaries by chemically tuning the composition. However, the complex chemical composition at the phase boundaries often reduces T_C (Fig. 4E). Our design strategy of constructing nanoscale structural and polar heterogeneity intrinsic to the nanopillar structure in NPR-NNO thin films has the advantage of improving the piezoelectric coefficient while simultaneously maintaining a high T_C (Fig. 4E). An additional advantage of the nanopillar approach is the simple chemical composition relative to other thin films (Fig. 4F and fig. S10B). Complex chemical compositions make phase boundary construction challenging because the dopant levels are only a few percent and often involve highly volatile elements (Na, K, Pb, and Bi). This presents an impediment to obtaining reliable and reproducible synthesis of bulk ceramics. Thin films are even more problematic to reliably synthesize. The NPR-NNO thin film contains only three elements, so our design strategy shows great potential for improving composition control to obtain high-performance piezoelectric thin films.

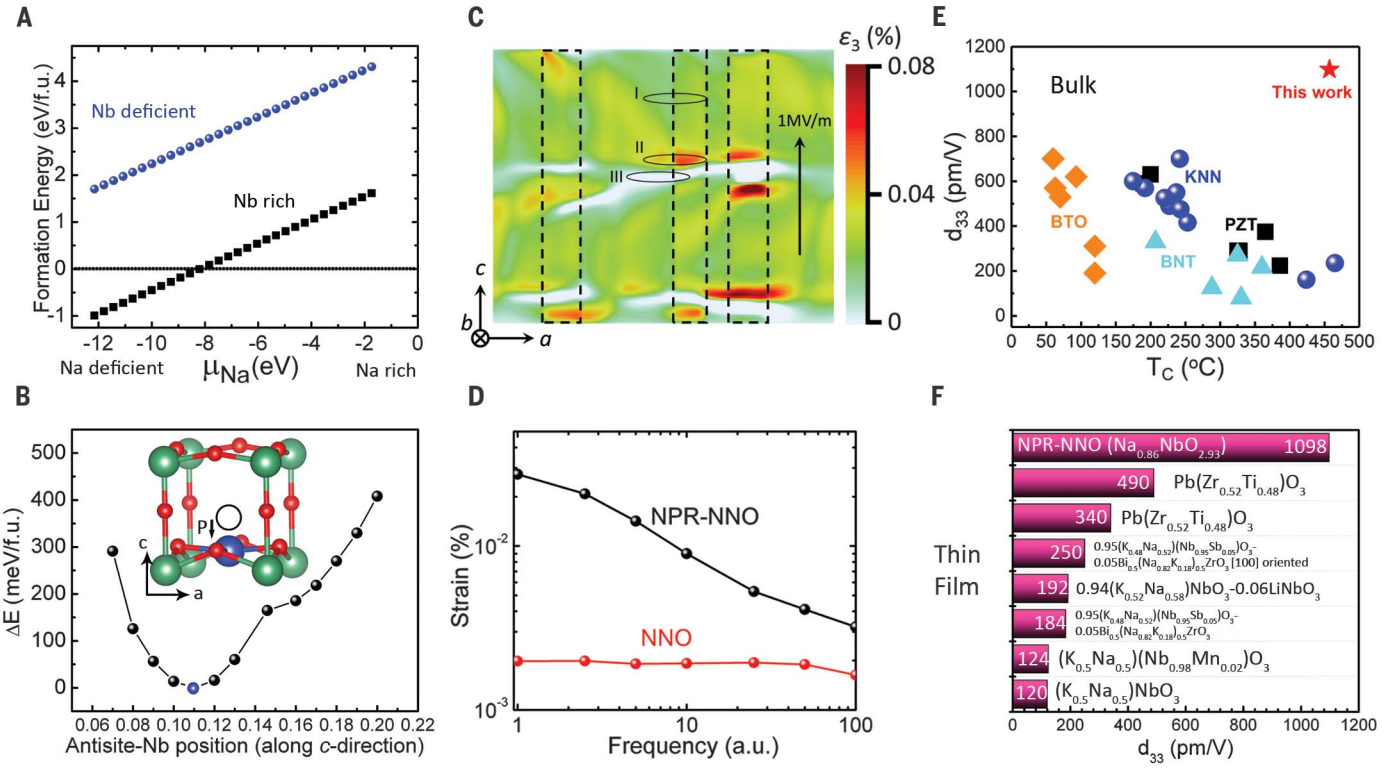

Fig. 4. Theoretical calculation and overview of piezoelectric properties. (**A**) Antisite formation energy as a function of the chemical potential of Na under Nb-rich and Nb-deficient conditions. (**B**) Energy curve of the antisite Nb atom at different positions along the out-of-plane *c* direction. The structural model in the inset illustrates the off-centering displacement of the antisite Nb atom (the blue sphere) in the lowest-energy position. Green spheres are regular Nb atoms; red spheres are oxygen atoms. (**C**) Mapping of the piezoelectric strain response of the NPR-NNO film under an applied electric field of 1 MV/m from phase-field simulation. Region I corresponds to the monoclinic domains, region II the domain wall regions, and region III the tetragonal domains. The dashed rectangles show the nanopillar regions. (**D**) Average piezoelectric strain response of the NPR-NNO and NNO films as a function of field frequency from phase-field simulation. (**E**) Comparison of piezoelectric coefficient d_{33} of bulk material systems with this work (thin film) as a function of Curie temperature T_C. PZT, $Pb(Zr_{0.52}Ti_{0.48})O_3$-based piezoelectric materials; BTO, $BaTiO_3$-based piezoelectric materials; BNT, $(Bi_{0.5}Na_{0.5})TiO_3$-based piezoelectric materials; KNN, $(K_{0.5}Na_{0.5})NbO_3$-based piezoelectric materials. (**F**) Piezoelectric coefficient of the NPR-NNO thin film with simple chemical composition compared to other piezoelectric thin films with much more complicated chemical compositions.

Furthermore, because the out-of-phase boundary can be coupled to magnetic (*26*) and superconducting properties (*27*), the formation of local heterogeneity through such nanopillar structures in perovskite oxides (ABO_3) with A-site deficiency could enable other emergent phenomena in functional materials.

REFERENCES AND NOTES

1. B. Jaffe, W. R. Cook, H. Jaffe, *Piezoelectric Ceramics* (Academic Press, 1971).
2. J. Wu, D. Xiao, J. Zhu, *Chem. Rev.* **115**, 2559–2595 (2015).
3. W. Liu, X. Ren, *Phys. Rev. Lett.* **103**, 257602 (2009).
4. J. Gao *et al.*, *Appl. Phys. Lett.* **99**, 092901 (2011).
5. F. Li *et al.*, *Nat. Mater.* **17**, 349–354 (2018).
6. Q. Liu *et al.*, *Energy Environ. Sci.* **11**, 3531–3539 (2018).
7. F. Li, S. Zhang, D. Damjanovic, L. Chen, T. R. Shrout, *Adv. Funct. Mater.* **28**, 1801504 (2018).
8. M. A. Zurbuchen *et al.*, *J. Mater. Res.* **22**, 1439–1471 (2007).
9. Z. Wang *et al.*, *Proc. Natl. Acad. Sci. U.S.A.* **115**, 9485–9490 (2018).
10. M. J. Marcinkowski, N. Brown, R. M. Fisher, *Acta Metall.* **9**, 129–137 (1961).
11. D. B. Holt, *J. Phys. Chem. Solids* **30**, 1297–1308 (1969).
12. M. D. Nguyen, E. P. Houwman, G. Rijnders, *Sci. Rep.* **7**, 12915 (2017).
13. Y. Wang *et al.*, *Adv. Electron. Mater.* **5**, 1800691 (2019).
14. See supplementary materials.
15. R. J. D. Tilley, *J. Solid State Chem.* **21**, 293–301 (1977).
16. T. Saito, T. Wada, H. Adachi, I. Kanno, *Jpn. J. Appl. Phys.* **43**, 6627–6631 (2004).
17. A. M. Glazer, *Acta Crystallogr. A* **31**, 756–762 (1975).
18. A. M. Glazer, *Acta Crystallogr. B* **28**, 3384–3392 (1972).
19. S. K. Mishra, N. Choudhury, S. L. Chaplot, P. S. R. Krishna, R. Mittal, *Phys. Rev. B* **76**, 024110 (2007).
20. K. Yao, F. E. H. Tay, *IEEE Trans. Ultrason. Ferroelectr. Freq. Control* **50**, 113–116 (2003).
21. L. Wang, K. Yao, W. Ren, *Appl. Phys. Lett.* **93**, 092903 (2008).
22. P. C. Goh, K. Yao, Z. Chen, *Appl. Phys. Lett.* **97**, 102901 (2010).
23. X. Ren, *Nat. Mater.* **3**, 91–94 (2004).
24. N. Bassiri-Gharb *et al.*, *J. Electroceram.* **19**, 47–65 (2007).
25. D. Lee *et al.*, *Science* **349**, 1314–1317 (2015).
26. T. Hibma *et al.*, *J. Appl. Phys.* **85**, 5291–5293 (1999).
27. J. Orenstein, A. J. Millis, *Science* **288**, 468–475 (2000).

ACKNOWLEDGMENTS

H.L. acknowledges helpful discussions with D. D. Fong and H. Zhou. **Funding:** Supported by the Institute of Materials Research and Engineering, A*STAR, RIE2020 AME Core Funds–SERC Strategic Funds: Seeding R&D Activities for Competitive Grants (grant A1718 g0056), National Research Foundation Competitive Research Programme grant NRF-CRP15-2015-04, and NSF grant DMR-1744213. Also supported by a Lee Kuan Yew Postdoctoral Fellowship through Singapore Ministry of Education Tier 1 grant R-284-000-212-114 (H.W.); Singapore Ministry of Education Tier 2 grant MOE2017-T2-1-129 (S.J.P. and H.W.); the Institute of High Performance Computing, Agency for Science, Technology And Research (IHPC, A*STAR) (K.P.O.); Singapore Ministry of Education AcRF Tier-2 grant MOE2019-T2-1-163 and Singapore National Research Foundation under its Competitive Research Funding R-398-000-087-281 (A.R.), and the Singapore Synchrotron Light Source (SSLS) via NUS Core Support Grant C-380-003-003-001, which is a National Research Infrastructure under the National Research Foundation, Singapore. Work at the University of Missouri (D.J.S.) is supported by the U.S. Department of Energy, Basic Energy Sciences, award DE-SC0019114. **Author contributions:** H.L. conceived the main idea, grew the films, and carried out the electric testing; H.L. and C.K.I.T. fabricated the ceramic targets; Y.F.C. deposited the electrodes; H.W. and Y.Z. performed aberration-corrected STEM and analyzed the data; H.L., P.Y., W.K.A.W., and E.P.C. performed x-ray diffraction and analyzed the data; P.K.D., C.D., and X.C. carried out x-ray spectroscopy and analyzed the data; K.P.O. performed DFT calculations and built theoretical models with input from H.L. and in discussion with D.J.S.; results of first-principles calculations were analyzed by K.P.O. and D.J.S.; T.Y. and L.-Q.C. performed and analyzed the phase-field simulations; K.Y. planned and guided the work, and analyzed the electric testing results; H.L., H.W., T.Y., D.J.S., S.J.P., A.R., M.B.H.B., and K.Y. wrote and modified the manuscript with input from others. All authors discussed the results and revised the manuscript. **Competing interests:** The authors have filed provisional Singapore Patent 10201908039P. **Data and materials availability:** All data are available in the main text and the supplementary materials.

SUPPLEMENTARY MATERIALS

science.sciencemag.org/content/369/6501/292/suppl/DC1
Materials and Methods
Figs. S1 to S10
References (*28*–*40*)

15 February 2020; accepted 19 May 2020
10.1126/science.abb3209